has a sinusoidal appearance, with multiple maxima repeating at regular harmonics of $\Delta\Omega_m$. (In the case of an ideal staircase record the sinusoidal curve would be replaced by a succession of evenly spaced sharp peaks.) Here $\Delta\Omega_m$ is determined more precisely and information can be extracted on the radial location $R_{eff}(\Omega)$ of the phase-slip site, to gain insight into the vortex formation process.

In ^{3}He-A, both $n = 1$ and $n = 2$ vortices exist. In our experimental conditions $n = 1$ vortices have the lowest energy[17]. However, it is not energy considerations but the critical properties which matter in the phase-slip process. An emerging new vortex is formed as an elementary vortex ring, comparable in size to the length scale which characterizes its structure. The appropriate length scale for the singular core of the $n = 1$ vortex is the superfluid coherence length ($\xi \approx 10$–100 nm), while for the $n = 2$ vortex it is the healing length of the $\hat{\mathbf{l}}$ texture ($\xi_D \gtrsim 10\,\mu$m). The critical flow velocity v_c for creating the elementary vortex ring is inversely proportional to its size[16] and is thus generally an order of magnitude larger for the $n = 1$ vortex. In this case it also depends on the surface roughness of the cylinder wall as the flow velocity is expected to reach its absolute maximum value in the vicinity of a sharp surface asperity (of approximate size ξ). In contrast, the soft-core of the $n = 2$ vortex is created deep in the bulk liquid, as seen in Fig. 4b. The site of this phase slip becomes Ω dependent, because the distance from the wall $R - R_{eff}$ is a significant fraction of the width $v_c/(2\Omega)$ of the vortex-free region around the vortex cluster (Fig. 2): when the width shrinks with increasing Ω the phase-slip centre is pushed closer to the wall.

Thus, when superfluid ^{3}He-A is slowly set into rotation, doubly quantized vortex lines are formed first and so the flow velocity never reaches high enough values for singly quantized events to become possible. This process can be understood as a macroscopic phase-slip phenomenon, as the full length of the vortex line is $\sim$1 cm and the Josephson period is larger than 1 s. The two circulation quanta of the vortex line correspond to a 4π phase winding around the vortex, which arises from a continuous orientational distribution over 4π of the orbital $\hat{\mathbf{l}}$ field within the vortex. □

Received 30 November 1999; accepted 16 February 2000.

1. Kléman, M. *Points, Lines, and Walls in Liquid Crystals, Magnetic Systems and Various Ordered Media* (Wiley, New York, 1983).
2. Hindmarsh, M. & Kibble, T. W. B. Cosmic strings. *Rep. Prog. Phys.* **58,** 477–562 (1995).
3. Tilley, D. R. & Tilley, J. *Superfluidity and Superconductivity* (IOP, New York, 1990).
4. Vollhardt, D. & Wölfle, P. *The Superfluid Phases of ^{3}He* (Taylor & Francis, London, 1990).
5. Matthews, M. R. *et al.* Vortices in a Bose–Einstein condensate. *Phys. Rev. Lett.* **83**, 2498–2501 (1999).
6. Onsager, L. *Nuovo Cimento* **6** (Suppl. 2), 249 (1949).
7. Feynman, R. P. *Progress in Low Temperature Physics* (ed. Gorter, C. G.) Vol. 1, 17–51 (North-Holland, Amsterdam, 1955).
8. Mermin, N. D. & Ho, T. L. Circulation and angular momentum in the *A* phase of superfluid helium-3. *Phys. Rev. Lett.* **36,** 594–597 (1976).
9. Ho, T. L. Spinor Bose condensates in optical traps. *Phys. Rev. Lett.* **81,** 742–745 (1998).
10. Achucarro, A. & Vachaspati, T. Semilocal and electroweak strings. *Phys. Rep.* (in the press); preprint hep-ph/9904229 at ⟨xxx.lanl.gov⟩ (1999).
11. Anderson, P. W. & Toulouse, G. Phase slippage without vortex cores: Vortex textures in superfluid ^{3}He. *Phys. Rev. Lett.* **38,** 508–511 (1977).
12. Volovik, G. E. & Kopnin, N. B. On rotating ^{3}He-A. *JETP Lett.* **25**, 22–24 (1977).
13. Hakonen, P. J., Ikkala, O. T. & Islander, S. T. Experiments on vortices in rotating superfluid ^{3}He-A. *Phys. Rev. Lett.* **49,** 1258–1261 (1982).
14. Seppälä, H. K. & Volovik, G. E. Evidence for nonsingular vorticity in the Helsinki experiments on rotating ^{3}He. *J. Low Temp. Phys.* **51,** 279–290 (1983).
15. Packard, R. E. The role of the Josephson-Anderson equation in superfluid helium. *Rev. Mod. Phys.* **70,** 641–651 (1998).
16. Ruutu, V. M. H., Parts, Ü., Koivuniemi, J. H., Kopnin, N. B. & Krusius, M. Intrinsic and extrinsic mechanisms of vortex formation in rotating superfluid ^{3}He-B. *J. Low Temp. Phys.* **107,** 93–164 (1997).
17. Parts, Ü *et al.* Phase diagram of vortices in superfluid ^{3}He-A. *Phys. Rev. Lett.* **75,** 3320–3323 (1995).

Acknowledgements

We thank H. Götz for help with the data analysis. This collaboration was carried out under the EU-TMR programme.

Correspondence and requests for materials should be addressed to V.B.E. (e-mail: ve@boojum.hut.fi).

Imaging of localized electronic states in the quantum Hall regime

N. B. Zhitenev*, T. A. Fulton*, A. Yacoby*†, H. F. Hess*‡, L. N. Pfeiffer* & K. W. West*

* *Bell Laboratories, Lucent Technologies, Murray Hill, New Jersey 07974, USA*
† *Weizmann Institute of Science, Rehovot 76100, Israel*
‡ *Phasemetrics Inc., San Diego, California 92121, USA*

The concept of electron localization has long been accepted to be essential to the physics of the quantum Hall effect[1,2] in a two-dimensional electron gas. The exact quantization of the Hall resistance and the zero of the diagonal resistance over a range of filling factors close to integral are attributed to the localization of electronic states at the Fermi level in the interior of the gas. As the electron density is changed, charging of the individual localized states may occur by single-electron jumps[3,4], causing associated oscillations in the local electrostatic potential. Here we search for such a manifestation of localized states in the quantum Hall regime, using a scanning electrometer probe[5,6]. We observe localized potential signals, at numerous locations, that oscillate with changing electron density. In general, the corresponding spatial patterns are complex, but well-defined objects are often seen which evidently arise from individual localized states. These objects interact, and at times form a lattice-like arrangement.

Recently, various scanning probe experiments[6,7,8] have been used to investigate the quantum Hall state on a micrometre scale, with some intriguing structure observed down to the 100-nm level[7]. We employ a single-electron transistor (SET) fabricated on the tip of a tapered glass fibre[6,9] as a scanning electrometer. The resistance of the SET is sensitive to the charge induced on its central island. The SET is placed above the surface of a GaAs/AlGaAs heterostructure that has a two-dimensional electron gas (2DEG) buried 100 nm below the surface. Moving the SET along the surface changes its resistance in response to the local electrostatic potential arising from the heterostructure. We map this potential by recording the feedback voltage (V_{fb}) applied to the heterostructure that keeps the induced charge on the central island of the SET constant[6], and thus also its resistance.

This heterostructure potential mainly comes from fixed charges (such as donors) above the 2DEG. We focus on the change in this potential ΔV that occurs when electron density n is changed (by voltage on the backgate). There are two expected contributions to ΔV. The main part is the local 2DEG contact potential which tracks the variation of the Fermi level with n. There may also be potential changes resulting from the charging of the localized states.

Under the quantum Hall conditions, as n is varied the ΔV changes rapidly in a step-like manner at n values that produce integer filling factors ν (defined as $\nu = nh/Be$ where B is the magnetic field, and h/e is the flux quantum), where the Fermi level passes between Landau levels. We have used[6] these potential steps as a marker to determine the spatial dependence of ν and, hence, density within the 2DEG. Now, employing higher resolution in position and density, we look for individual localized states in regions of almost-integer filling factor.

In our experiments, B is set at a fixed value near $\nu = 2$ or $\nu = 1$. We place the SET at a fixed, arbitrary point and record V_{fb}, the d.c. measurement of ΔV; the electron density is swept by a voltage V_{bg} applied to the backgate. We also use V_{bg} to modulate n at a frequency above the roll-off of the feedback loop and we record the equivalent 'transparency' signal, the a.c. potential seen by the SET, which has a better signal-to-noise ratio. Alternatively, instead of sweeping density, we record a set of spatial images of these signals at various

fixed V_{bg}. As will be seen, these signals show marked variation on spatial scales down to ~100 nm and, notably, for density changes of less than 1 electron μm^{-2}.

Broadly, the density dependence of the signals tends to be one of two types, as shown in the examples in Fig. 1a for $\nu = 2$. Both d.c. signals, taken at different locations, display the expected step of $\sim h\omega_c/2\pi$, where ω_c is the cyclotron frequency, at $\nu = 2$ (refs 6 and 10). The amplitudes of the associated transparency signals, however, differ greatly. The smaller signal in the right panel quantitatively corresponds to the derivative of the d.c. step, unlike the much larger signal in the left panel. Such an excessive transparency signal indicates that an equilibrium charge density is not established (at 70 Hz), owing to resistive effects. This is supported by detection of an out-of-phase signal component. We now consider only cases where the transparency shows equilibrium charging behaviour.

Figure 1b shows a representative set of such transparency curves taken at a grid of points spaced by 0.1 μm. No accompanying out-of-phase signal is seen. The middle of the associated d.c. steps corresponds to a local filling factor $\nu = 2$, giving a local density of $2B/(h/e)$ at the respective values of V_{bg}. All of these transparency signals display multiple oscillations with peaks separated by 20–40 mV in V_{bg}. Such patterns are largely reproducible in successive measurements, although they change slowly over time. In places, the transparency oscillations reach definite, reproducible, negative values. The spatial correlation length for the individual oscillation peaks is short and hard to quantify. Where peaks can be followed between adjacent points, they seem to shift in V_{bg}. As noted above, the integrated transparency signals reproduce the respective d.c. steps, but with a superior signal-to-noise ratio. In the integration, the oscillations result in small (~0.5 mV) step-like corrugations superimposed on the broader d.c. step of $h\omega_c/2\pi$. The measured d.c. signals sometimes show this multiple-step structure, but usually it is obscured by noise. At a given point, these oscillations in the transparency are observed over a total density change of ~2–4%, or 30–60 electrons μm^{-2}.

The spatial maps of the transparency in such regions usually show rather complex patterns that change rapidly with density. However, if the oscillations with density are well defined, there is often a simpler spatial pattern. An example is shown in Fig. 2. The transparency of the 0.5×0.5 μm^2 scanned area is shown for five successive additions of ~1.3 electrons μm^{-2}. There are clearly seen ring-like structures contracting into a common centre. The pattern almost repeats over three cycles of oscillation as the density is increased (only part of the evolution is shown), with a period of ~4 electrons μm^{-2}. Taken together, the ring size and the density period suggest that this cyclic behaviour involves the addition of a single electronic charge to the associated area. Clearly, such patterns provide the spatial visualization for the 'sliding' peaks seen in the density curves. We have seen many such contracting ring patterns, which more often show one to two cycles of repetition, but no clear examples of expanding rings. The rings and other associated patterns may appear anywhere across the region of the step in d.c. potential, both in the steeper part and in the tails.

The more complex transparency patterns often appear to contain multiple interacting and distorted ring-like objects. Particularly clear are the networks, such as appear in some of the 1×1 μm^2 panels of Fig. 3. These are taken near $\nu = 1$, at increments of 0.65 electrons μm^{-2}. The individual cells tend to be hexagonal, but not identical. In the sequence, the network is initially well formed, then falls apart. At a higher density, a new, denser pattern of cells forms in the same area (Fig. 3e), which again persists over a short range of density. The density of cells is ~15–30 μm^{-2}, consistent with the charge density given by the estimated departure from integer filling

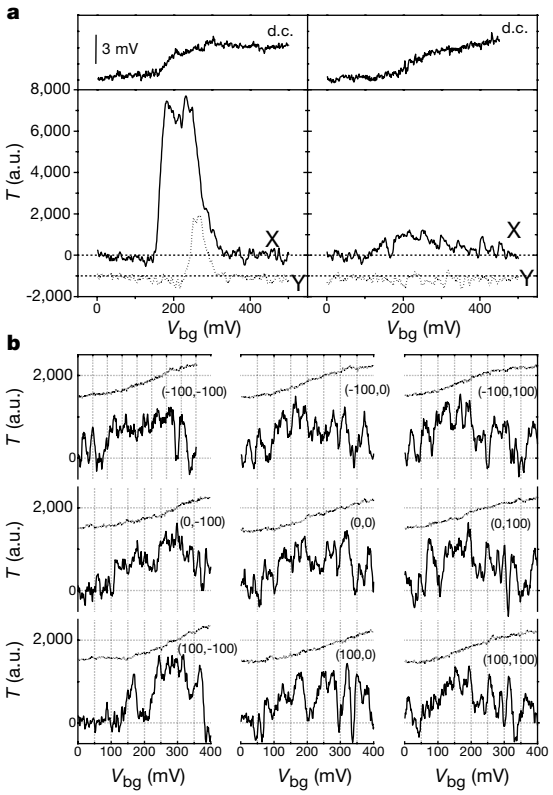

Figure 1 The d.c. and transparency signals at fixed points. **a**, Equilibrium versus non-equilibrium charging. Two typical sets of data (left and right panels) acquired by the single-electron transistor as the electron density ($\sim V_{bg}$) is swept through $\nu = 2$ at different spatial locations. The electron density n is $\sim 1.5 \times 10^{11}$ cm^{-2}, and varies by a few per cent with location. A backgate bias $V_{bg} = -1$ V reduces n by 1.3×10^{10} cm^{-2}. Upper traces: d.c. signal displaying the characteristic step of the contact potential as the Fermi level moves between the Landau levels. Lower traces: in-phase component (X) and out-of-phase component (Y) (shifted down by 1,000) of transparency signal. The large transparency on the left panel is characteristic of non-equilibrium charging at 70 Hz. The smaller, completely in-phase transparency on the right panel signifies equilibrium charging. **b**, Rapid variation of transparency with density and position. The d.c. (upper traces) and in-phase transparency (lower traces) signals are plotted as a function of V_{bg} measured at nine spatial locations arranged in a 3×3 grid over an area of 0.2×0.2 μm^2. The middle of the d.c. steps serve as an estimate for the local $\nu = 2$ condition. Multiple oscillations seen in transparency signal are reproducible. No out-of-phase transparency signal is detected. All measurements shown are carried out at a temperature of 0.8 K.

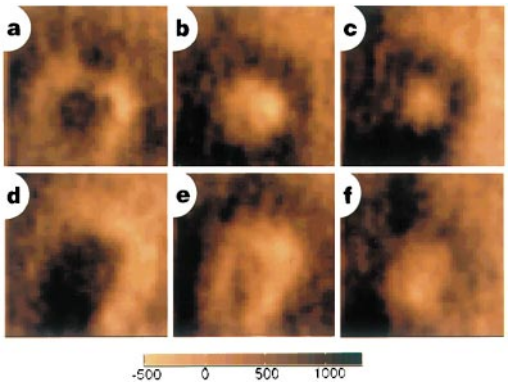

Figure 2 Spatial images of the transparency at $\nu = 2$ showing single-electron rings. **a–f**, Images of 0.5×0.5 μm^2 area are taken at six increasing densities. V_{bg} is changed by 10 mV between images which adds ~0.3 electron charges to the area of the panel. The transparency signals on the rings (light areas) are comparatively small, and sometimes negative (an overscreening of the a.c. backgate voltage), whereas those in the centre of the rings (dark regions) are larger and positive (an underscreening of the signal).

factor. This further suggests a direct relation between the cells and single-electron states.

Figure 4 shows the evolution of a portion of such a network in which the transition between the cells and isolated rings is seen. The successive images involve an addition of ~0.16 electrons to the area shown. Initially the structure has nearly triangular cells, but they change to a more hexagonal shape in Fig. 4b. In Fig. 4c and d the pattern shifts and the individual cells change in size. The cells separate as they shrink further in size (Fig. 4e), and they take on a ring-like form, a process which continues in Fig. 4f. The visual impression is that the rings are structures that have an individual identity. They have an elastic nature, in that they flatten out by mutual short-range repulsion when brought into contact, and take a circular shape when not actually touching. They have not been seen to merge. Many similar networks have been seen, both near $\nu = 1$ and, in less detail, near $\nu = 2$.

We took special care to test whether these spatial patterns could be induced by a gating effect of the tip. In all the experiments shown, the d.c. bias on the SET is set to nullify the contact potential. To do this, we adjust the voltage between the SET and the 2DEG to minimize the charge induced on the SET as the tip is lowered to the working height. During the spatial imaging, the effective gating voltage of the SET is less than 30 mV, ensuring that the amount of charge induced on the 2DEG by the SET is less than 0.5 electrons. In the test, the imaging of an area containing rings is then repeated with the tip biased off the original setting by 100–200 mV, so that the SET induces additional electrons or holes in the 2DEG. Such biased images display a different phase of the ring transformation but, qualitatively, the evolution of the ring pattern with density remains intact. We conclude that the ring patterns are not noticeably disturbed by the scanning tip. In addition, it seems improbable that well-developed networks of interacting rings such as occur in Figs 3 and 4 could be produced by a tip-gating effect.

The multiple oscillations of the transparency observed at a fixed spatial point are reminiscent of single-electron effects in quantum dots. There the analogous Coulomb-blockade charging behaviour is step-like changes in charge and an accompanying saw-tooth pattern of d.c. potential. When differentiated with respect to density, the d.c. saw-tooth yields an oscillating a.c. signal with negative regions, as indeed is seen here. Other experimental facts also strongly suggest that single-electron charging is involved. First, as mentioned above, the period of the cyclic contraction of the rings approximately corresponds to the addition of a single-electron charge over the area of the structure. Second, charge variations of $\sim e$ over a typical area of the rings are required to produce the multiple d.c. steps of the observed ~0.5 mV magnitude.

However, the complete set of properties cannot be accounted for by assuming the discrete charging of isolated localized states. We see no well-defined 'quantum dots' of constant shape. Although in some manner the collapsing of a ring through one cycle adds one electron to the immediate area, how this takes place is not clear. A Coulomb blockade model in which the electron is transferred into a fixed potential minimum created by disorder does not provide a continuous spatial variation in signal. A possible way to improve the fixed potential model is by incorporating interaction with other available electrons. It is broadly accepted, however, that the density of electrons available for screening is determined by the deviation from integer filling factor[11,12]. The total density range of the non-zero transparency is about $\sim 3 \times 10^9$ cm^{-2}, yielding an average distance between screening electrons of more than 200 nm. This distance is comparable to typical sizes of the ring patterns and to the distance between the cells in Figs 3 and 4. It is not clear how the continuous variation of the potential required by the ring can be provided with so few 'free' carriers. It is also difficult to understand how the network of interacting rings can develop within this model. For example, the positions of the cells in the network pattern seem to be dictated entirely by the neighbouring cells.

The continuous spatial variation of the rings, and even more so the network patterns, suggests an analogy with the continuous modulation of density that occurs in the Wigner crystal or in a charge-density wave. In such a case, the disorder potential is of secondary importance, primarily causing pinning, whereas the electron interactions define the overall evolution of the patterns. Indeed, we do not observe any correlation between the ring centres and the extrema of the surface potential. So far we are not able to develop this analogy to a reasonable model. Although it is tempting to identify the network with a small Wigner crystallite, this is premature. The ordering of the Wigner crystal originates from long-range interaction between electrons. The interaction between the cells of our networks appears to be of short range, implying that the cells (and the rings) are dipole objects. □

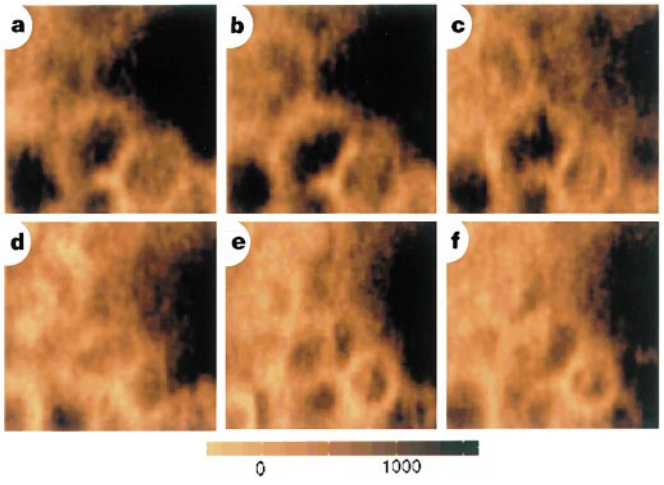

Figure 3 Interacting rings. **a–f**, Spatial images of the transparency signal over 1.0×1.0 μm^2 area taken at six increasing densities. V_{bg} is changed by 5 mV between images which adds ~0.65 electron charges to the area of the panel. Filling factor is close to 1. As in Fig. 2, the transparency signals are large and positive in the centre of the cells, and small, or even negative, on the cell boundaries.

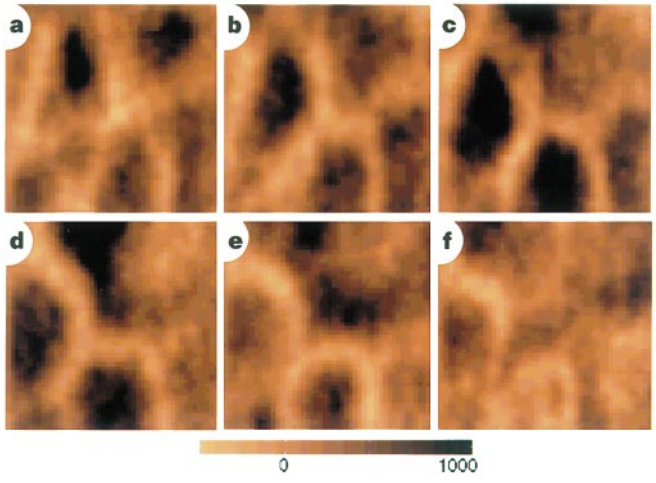

Figure 4 Close-up of colliding rings. **a–f**, Spatial images of the transparency signal over an area of 0.5×0.5 μm^2 taken at six increasing densities. V_{bg} is changed by 5 mV between images which adds ~0.16 electron charges to the area of the panel. Filling factor is close to 1.

Received 22 June 1999; accepted 6 January 2000

1. Prange, R. E. & Girvin, S. M. (eds) *The Quantum Hall Effect* (Springer, New York, 1990).
2. Laughlin, R. B. Quantized Hall conductivity in two dimensions. *Phys. Rev. B* **23,** 5632–5634 (1981).
3. Shklovskii, B. I. & Efros, A. L. *Electronic Properties Of Doped Semiconductors* (Springer, Berlin, 1985).
4. Kastner, M. A. Artificial Atoms. *Phys. Today* **46,** 24–31 (1993).
5. Yoo, M. J. *et al.* Scanning single-electron transistor microscopy: imaging individual charges. *Science* **276,** 579–582 (1997).
6. Yacoby, A. *et al.* Electrical imaging of the quantum Hall state. *Solid State Commun.* **111,** 1–13 (1999).
7. Tessmer, S. H. *et al.* Subsurface charge accumulation imaging of the quantum Hall liquid. *Nature* **392,** 51–55 (1998).
8. McCormick, K. L. *et al.* Scanned potential microscopy of edge and bulk currents in the quantum Hall regime. *Phys. Rev. B* **59,** 4654–4657 (1999).
9. Fulton, T. A. & Dolan, G. J. Observation of single-electron charging effects in small tunnel junctions. *Phys. Rev. Lett.* **59,** 109 (1987).
10. Smith, T. P. *et al.* Direct measurement of the density of states of a two-dimensional electron gas. *Phys. Rev. B* **32,** 2696–2699 (1985).
11. Efros, A. L. Density of states of 2D electron gas and width of the plateau of IQHE. *Solid State Commun.* **65,** 1281 (1988).
12. Efros, A. L. Non-linear screening and the background density of states of 2DEG in magnetic field. *Solid State Commun.* **67,** 1019–1022 (1988).

Acknowledgements

We thank L. Levitov, S. Simon, L. Balents and C. Varma for useful discussions.

Correspondence and requests for materials should be addressed to N. Z. (e-mail: zhiten@physics.bell-labs.com).

Anisotropic spinodal dewetting as a route to self-assembly of patterned surfaces

A. M. Higgins & R. A. L. Jones

Department of Physics and Astronomy, University of Sheffield, The Hicks Building, Sheffield S3 7RH, UK

The ability to pattern surfaces on a microscopic length scale is of importance for technological applications such as the fabrication of microelectronic circuits and digital storage media. Devices fabricated entirely from polymers are now available, opening up the possibility of adapting polymer processing technologies to fabricate cheap, large-area devices using non-lithographic techniques[1,2]—for example, by exploiting dewetting[3] and phase separation[4–6] in thin films. But the final pattern adopted by the polymer film using such approaches requires a template printed onto the substrate by optical lithography, microcontact printing[4,5] or vapour deposition[3]. Here we describe a simple process for patterning surfaces that does not require a template. Our method involves the spinodal dewetting of a polymer surface by a thin polymer film, in which a liquid film breaks up owing to the amplification of thermal fluctuations in film thickness induced by dispersion forces[7–14]. A preferred orientation is imposed on the dewetting process simply by rubbing the substrate, and this gives rise to patterns of remarkably well-aligned polymer lines. The width of these lines is well-defined, and is controlled by the magnitude of the dispersion forces at the interface, which in turn can be varied by varying the thickness of the polymer substrate. We expect that further work will make it possible to optimize the degree of order in the final morphology.

Previous work has shown that thin films of poly(methyl methacrylate) (PMMA) on polystyrene (PS) substrates are unstable with respect to spinodal dewetting[9]. We prepared bilayers of PMMA on PS as follows. First, PS (M_n = 248,900, M_w/M_n = 1.04, Polymer Source Inc., Canada) was applied by spin-coating toluene solutions of this compound onto silicon substrates. (Here M_n and M_w are respectively the number- and the weight-average molecular masses.) After removing residual solvent, the film thickness was measured by ellipsometry. Second, the PMMA layer was added by spin-coating a PMMA solution onto cleaved mica, and then floating the resulting film onto water and depositing this on top of the silicon/PS samples. Dewetting was observed by annealing the samples at 150 °C on a hot-stage in an optical microscope in reflection mode (Nikon ME600D). The experiments on isotropic samples were performed twice, using PMMA of two slightly different molecular masses (M_n = 102,700, M_w/M_n = 1.09, Polymer Source Inc.; M_n = 138,256, M_w/M_n = 1.04, Polymer Laboratories Ltd, UK). In each case, three different thicknesses of PS were used, a single PMMA film being deposited onto all three and also onto a bare silicon fragment with a known oxide thickness (this was used to measure the PMMA film thickness). Each sample was annealed until dewetted morphologies were clearly visible. In each case, annealing was stopped as soon as sufficient contrast was obtained to provide good quality images but before any coarsening of the morphology took place. For the samples annealed here this meant annealing times of one hour or less (significant coarsening does not occur until after several hours). For each thickness of PS, a silicon/PS sample was also annealed to check that this did not dewet on its own. On the timescales of the experiments, no dewetting was seen on any of the silicon/PS samples.

Figure 1a shows the typical morphology for a PS thickness of 1,750 Å. This is a characteristic pattern resulting from isotropic spinodal dewetting; the pattern is clearly characterised by a single length-scale, but is isotropic. This is made clearer by taking a Fourier transform of the image. To obtain fast Fourier transforms (FFTs) of the dewetted structures, photographs were taken at lower magnification (×20 objective) than that used in Fig. 1a, at a number of different places on each sample. Each photo was decomposed into red, green and blue colour channels, and FFTs were taken of each colour channel. The FFTs were then radially averaged. A typical FFT for the 1,750-Å PS sample is shown in Fig. 1b. The well-defined ring

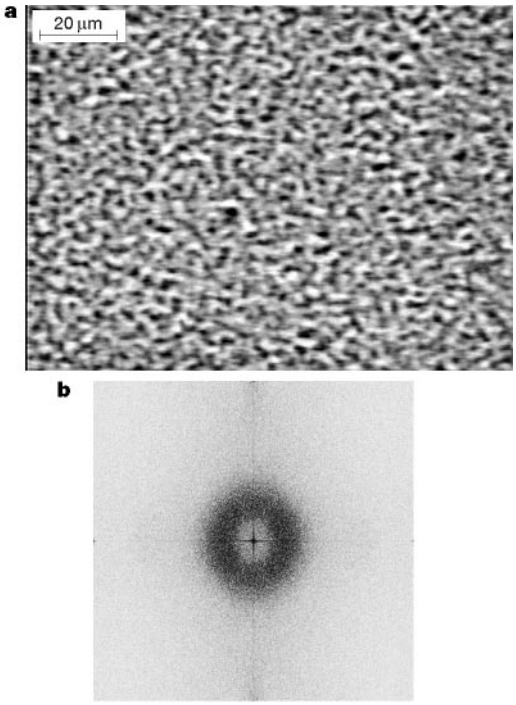

Figure 1 Dewetted morphology of a Si/PS/PMMA sample, where the PMMA film was prepared on cleaved mica. **a**, Optical micrograph of an annealed Si/PS/PMMA sample with a PS film thickness of 1,750 Å and a PMMA film thickness of 123 Å. **b**, Fast Fourier transform of a red-colour-channel image from this sample.